

## Vacancy-induced mechanical stabilization of cubic tungsten nitride

Karthik Balasubramanian,<sup>1</sup> Sanjay Khare,<sup>2</sup> and Daniel Gall<sup>3</sup>

<sup>1</sup>*Department of Mechanical, Nuclear and Aerospace Engineering, Rensselaer Polytechnic Institute, Troy, New York 12180, USA*

<sup>2</sup>*Department of Physics and Astronomy, The University of Toledo, 2801 West Bancroft Street, Toledo, Ohio 43606, USA*

<sup>3</sup>*Department of Materials Science and Engineering, Rensselaer Polytechnic Institute, Troy, New York 12180, USA*

(Received 27 July 2016; revised manuscript received 7 October 2016; published 18 November 2016)

First-principles methods are employed to determine the structural, mechanical, and thermodynamic reasons for the experimentally reported cubic WN phase. The defect-free rocksalt phase is both mechanically and thermodynamically unstable, with a negative single crystal shear modulus  $C_{44} = -86$  GPa and a positive enthalpy of formation per formula unit  $H_f = 0.623$  eV with respect to molecular nitrogen and metallic W. In contrast, WN in the NbO phase is stable, with  $C_{44} = 175$  GPa and  $H_f = -0.839$  eV. A charge distribution analysis reveals that the application of shear strain along [100] in rocksalt WN results in an increased overlap of the  $t_{2g}$  orbitals which causes electron migration from the expanded to the shortened W-W (110) bond axes, yielding a negative shear modulus due to an energy reduction associated with new bonding states 8.1–8.7 eV below the Fermi level. A corresponding shear strain in WN in the NbO phase results in an energy increase and a positive shear modulus. The mechanical stability transition from the NaCl to the NbO phase is explored using supercell calculations of the NaCl structure containing  $C_v = 0\% - 25\%$  cation and anion vacancies, while keeping the N-to-W ratio constant at unity. The structure is mechanically unstable for  $C_v < 5\%$ . At this critical vacancy concentration, the isotropic elastic modulus  $E$  of cubic WN is zero, but increases steeply to  $E = 445$  GPa for  $C_v = 10\%$ , and then less steeply to  $E = 561$  GPa for  $C_v = 25\%$ . Correspondingly, the hardness estimated using Tian's model increases from 0 to 15 to 26 GPa as  $C_v$  increases from 5% to 10% to 25%, indicating that a relatively small vacancy concentration stabilizes the cubic WN phase and that the large variations in reported mechanical properties of WN can be attributed to relatively small changes in  $C_v$ .

DOI: [10.1103/PhysRevB.94.174111](https://doi.org/10.1103/PhysRevB.94.174111)

### I. INTRODUCTION

Transition-metal nitrides have gained considerable interest due to their excellent mechanical properties, thermal stability, and corrosion resistance [1–9], and are widely used as hard wear-resistant coatings, diffusion barriers, and protective decorative coatings [2,3,6,8–13]. While TiN is the most studied transition-metal nitride and is used in all of the above applications, WN is relatively unexplored and its processing-structure-property relationships as well as its phase stability are not fully established yet. WN has potentially promising properties as its six valence electrons result in a high valence electron density, with three electrons per formula unit occupying metal  $d$  bands. This is expected to result in a relatively high ductility and a corresponding high toughness [14–19], but also results in a destabilization of the cubic rocksalt structure [20].

Tungsten nitride crystallizes in a wide range of phases with various anion-to-cation ratios, including cubic WN,  $W_2N$ , and  $W_3N_2$ , hexagonal  $W_2N$ ,  $W_5N_4$ , and  $W_5N_8$ , and rhombohedral  $W_7N_6$ , which form depending on the chosen processing parameters including temperature and  $N_2$  flow rate during deposition from the vapor phase [21–26]. In addition, synthesis at 5 GPa has been reported to yield high-pressure phases including hexagonal and rhombohedral  $W_2N_3$  and cubic  $W_3N_4$  [27]. Theoretical studies have predicted the thermodynamically most stable WN phase to be the hexagonal close-packed NiAs structure [28], the simple hexagonal WC phase [29] which is also experimentally observed at a pressure of 5 GPa [27], or more recently the NbO phase [20,30]. These latter studies have concluded that all phases except the NbO phase are thermodynamically unstable against phase separa-

tion into metallic W and molecular nitrogen. Nevertheless, experimentally, a large number of WN phases have been reported. Diffraction results suggest that cubic stoichiometric WN exhibits a rocksalt phase [21,31] while, in fact, the NbO phase has not been experimentally confirmed, yet. The absence of an experimental observation of WN in the NbO structure raises the question if kinetic barriers limit its formation or if entropy may favor a more random structure of WN. In that context, it is particularly interesting to directly compare stoichiometric WN in the NaCl and NbO structures. Both crystal structures are cubic and exhibit anion and cation sites on the same fcc sublattices. However, while all 4+4 lattice sites are occupied in the conventional cubic unit cell of the NaCl structure, the NbO structure has only three cations and three anions per cubic unit cell, exhibiting a regular array of both cation and anion vacancies that represent 25% of sites in comparison to the NaCl structure. First-principles calculations have predicted that WN in the NbO structure is mechanically stable, while it is unstable when crystallizing in the rocksalt structure [20,30]. This is interesting since reduced mechanical stability of other transition-metal carbides and nitrides [15,32–35] has been attributed to increasing valence electron concentrations which start to fill  $d-t_{2g}$  metallic states. However, since both the NbO and the rocksalt phase of WN share the same valence electron concentration per formula unit, it is interesting that one phase exhibits instability while the other is stable.

The question regarding the details of the mechanical stability of WN in the NbO, NaCl, or any intermediate cubic phase is also interesting as it may shed light on the reasons for the extremely large range of reported values for the WN elastic modulus  $E = 240 - 430$  GPa [21,24,31,36–38] and hardness

$H = 5 - 39$  GPa [25,31,36–40]. Some of this variation may be attributed to microstructural effects and deviations from stoichiometry. However, the large range of elastic moduli is particularly fascinating and requires a detailed understanding of the effect of vacancies on the mechanical properties, since the only difference between the NbO and the NaCl structure is the density of vacancies. Previous studies have investigated the effect of cation and anion vacancies on the elastic properties of NbN [41], HfN [42], and TiN [43], and on stabilizing metastable structures of  $\text{Ti}_{1-x}\text{Al}_x\text{N}$  [44],  $\text{Mo}_{1-x}\text{Al}_x\text{N}$  [45], and  $\text{Ti}_x\text{W}_{1-x}\text{B}_2$  [46]. Hence, a study of the mechanical and structural properties in the presence of a varying vacancy concentration and diverse vacancy configurations is pertinent to understand the growth and synthesis of tungsten nitride with desired mechanical properties and temperature stability.

In this paper, we present results from first-principles calculations that compare structural and mechanical properties of WN in the rocksalt and NbO phases. WN in the rocksalt phase is found to be mechanically and thermodynamically unstable, with a negative  $C_{44}$  of  $-86$  GPa and a corresponding negative isotropic elastic modulus of  $-285$  GPa. Electron-density surfaces and total electron density of states of relaxed and strained structures suggest that the reason for the instability is associated with electron migration from W-W bonds along  $[110]$  to W-W bonds along  $[1\bar{1}0]$  during shearing, causing migration of electrons to deeper energy levels which results in a lower total energy and, in turn, a negative shear modulus. However, the introduction of vacancy pairs on 5% of anion and cation sites causes mechanical stabilization, with the most stable cubic WN phase, the NbO phase, having 25% of vacancies resulting in a positive  $C_{44} = 175$  GPa and  $E = 561$  GPa. The results indicate that the vacancy concentration in WN dramatically affects the mechanical properties with, for example, a predicted hardness that increases from zero to 26 GPa, providing insight into the possible reasons for the large range of reported mechanical properties of WN.

## II. COMPUTATIONAL PROCEDURE

First-principles density functional calculations were performed using the Vienna *ab initio* simulation package (VASP), employing periodic boundary conditions, a plane-wave basis set, the Perdew-Burke-Ernzerhof generalized gradient approximation exchange correlation functional [47], and the projector-augmented wave method [48]. All computational parameters are chosen such that calculated total energy differences are converged to within 1 meV/atom. This includes a 500 eV cut-off energy for the plane-wave basis set expansion and a  $\Gamma$ -centered  $20 \times 20 \times 20$   $k$ -point grid for conventional unit cells containing six to eight atoms, and a  $5 \times 5 \times 5$   $k$ -point grid for cubic  $2 \times 2 \times 2$  supercells with 32 cation and 32 anion sites that are occupied by 48–64 W and N atoms. W  $6s, 5p$ , and  $5d$  electrons are explicitly calculated, that is, they are not included in the pseudopotential. Atomic positions and lattice parameters were relaxed until an energy convergence of  $10^{-4}$  eV was reached, while keeping the unit-cell shape fixed. More specifically, this was done by multiple calculations for each atomic configuration, where atoms were relaxed at a fixed lattice parameter that was varied for the different calculations by 0.01 Å increments. Subsequently, the relaxed lattice

constant and corresponding energy was determined by fitting the calculated energy vs lattice parameter with a second order polynomial. The enthalpy of formation  $H_f$  of a configuration is determined using  $H_f = (E_{\text{configuration}}/n) - (E_W + E_N)$ , where  $E_{\text{configuration}}$  is the total energy calculated for a particular configuration,  $n$  is the number of tungsten or nitrogen atoms,  $E_W = -12.957$  eV is the calculated enthalpy per atom of bulk bcc tungsten, and  $E_N = -8.317$  eV is half the enthalpy of a nitrogen molecule. We note, the values for  $E_W$  and  $E_N$  are the enthalpies relative to the pseudoatoms for which the pseudopotentials were created within the VASP package, that is, a not spin-polarized W atom with five  $5d$  electrons and only one  $6s$  electron, and a not spin-polarized N atom.

Thermodynamically stable phases are identified by employing the evolutionary algorithm USPEX [49–51] coupled with first-principle calculations at 0 K and 0 GPa. A fixed composition search was carried out with the total number of atoms varying from 2 to 14 atoms with elemental tungsten and nitrogen as building blocks and the ratio of tungsten to nitrogen set to unity. Simulations were carried out until the most stable phase remained unchanged for ten consecutive generations, corresponding to exploring a total of 115 different structures.

The three independent elastic constants  $C_{11}$ ,  $C_{12}$ , and  $C_{44}$  are determined by applying a set of strains to the conventional unit cell, and fitting second order polynomial functions to the calculated elastic energy vs strain. In particular,  $C_{11}$  is determined from tensile and compressive  $\pm 1\%$ – $3\%$  strains along  $[001]$ ,  $C_{12}$  is calculated from the bulk modulus  $B$  using  $C_{12} = (3B - C_{11})/2$  [52], where  $B$  is obtained from a fit of the calculated energy vs lattice constant using the Murnaghan equation of state, and  $C_{44}$  is determined using a  $1\%$ – $5\%$  shear strain along  $[100]$ . For configurations that do not exhibit cubic symmetry,  $C_{11}$ ,  $C_{22}$ , and  $C_{33}$  are individually determined to subsequently determine their average  $\overline{C_{11}}$ . Similarly,  $C_{12}$ ,  $C_{23}$ , and  $C_{31}$  are averaged to obtain  $\overline{C_{12}}$ , and  $C_{44}$ ,  $C_{55}$ , and  $C_{66}$  are averaged to obtain  $\overline{C_{44}}$ . These “pseudocubic” averages are subsequently used to determine isotropic constants with relations that assume cubic symmetry. The isotropic elastic modulus  $E$  and isotropic shear modulus  $G$  are obtained from the calculated elastic constants using Hill’s approximation [53]. The Pugh’s ratio  $k$  and isotropic Poisson’s ratio  $\nu$  are calculated using  $k = G/B$  and  $\nu = (E/2G) - 1$  [54]. The Vicker’s hardness is then calculated according to Tian’s model  $H_v = 0.92k^{1.137}G^{0.708}$  [55].

The ideal tensile strength along  $\langle 001 \rangle$ ,  $\langle 110 \rangle$ , and  $\langle 111 \rangle$  is calculated by applying a tensile strain along the respective directions and letting the other strain components relax until the orthogonal stress components are less than 0.5 GPa. Similarly, the ideal shear strength along  $(111)[1\bar{1}\bar{2}]$  and  $(010)[001]$  is calculated by orienting the crystal with coordinate axes parallel and perpendicular to the slip plane and applying strains along the coordinate axes and letting the other strain components relax until all the stress components except the component of interest is less than 0.5 GPa.

Electron-density difference maps are created by calculating the charge density within the conventional unit cell using a  $65 \times 65 \times 65$  mesh. Subsequently, the charge density distributions of isolated W and N atoms located at the same positions as those within the calculated unit cell are subtracted

from the charge density in order to highlight the change in electron density associated with atomic bonding. Contour plots of the electron density difference for specific crystalline planes are obtained by taking cuts of the overall electron density difference at specific planes. The schematics of the rocksalt and the NbO phase are visualized using VESTA [56].

The electronic density of states (DOS) is calculated using conventional unit cells with eight or six atoms for the NaCl or NbO structures, respectively, using the tetrahedron method with Blöchl corrections [57] for energy smearing in a dense mesh of  $20 \times 20 \times 20$   $k$  points. The DOS is determined for a total of 2200 energy points from 20 eV below to 2 eV above the Fermi level, corresponding to an energy resolution of 10 meV. The site projected DOS is obtained by projecting the wave functions of each band onto local orbitals around each ion.

The effect of the vacancy concentration in cubic stoichiometric WN is explored using  $2 \times 2 \times 2$  supercells containing 32 cation and 32 anion sites arranged in a regular NaCl lattice. The sites are filled with 23 to 32 W and N atoms, respectively, keeping the N-to-W ratio constant at unity. This is done by simultaneously removing both W and N atoms, yielding a vacancy pair concentration  $C_v = 0 - 0.28$ . For each value of  $C_v$ , multiple atomic configurations are generated by adding vacancy pairs to the regular NaCl-structure lattice through the following three routes. (i) Configurations where the vacancies occupy a subset of the same lattice sites that are also in the NbO structure: These configurations are obtained by removing W and N atoms from the NbO structure vacancy sublattice. For each  $C_v$ , all possible arrangements of vacancies on this sublattice consisting of eight cation and eight anion sites within a  $2 \times 2 \times 2$  supercell are computed. For  $C_v = 0.28$ , all four configurations of a vacancy pair in addition to the eight cation and eight anion vacancies in the NbO phase of WN are investigated. (ii) High-symmetry and ordered configurations which are somewhat arbitrarily chosen by the authors, based on our expectations that anion or cation vacancy clustering along low index directions such as  $\langle 100 \rangle$  and  $\langle 110 \rangle$  or in low index planes such as  $(111)$  or  $(110)$  may correspond to low energy configurations. This “manual” method is also used to generate all three configurations for a single vacancy pair within the supercell. (iii) Configurations with randomly arranged vacancy pairs: for each  $C_v$ , five configurations were created by randomly removing W and N atoms from the 64-atom unit cell. A total of 75 configurations were generated with the above methods (i)–(iii). Their formation enthalpy was calculated by allowing their atoms and lattice constants to relax to the ground state, while keeping the unit cell shape fixed as a cubic supercell. Subsequently, the lowest-energy configuration for each  $C_v$  was further investigated. In particular, the elastic constants and hardness were calculated using the above-described approach.

The distribution of the number of nearest neighbors in the random structures was quantified to confirm that they agree with the expected values for a true random vacancy distribution. This approach follows the general arguments for the creation of special quasirandom structure supercells [58], where a structure that matches the expected neighbor distribution for a random configuration is expected to exhibit physical properties that approximate the true random configuration. For

the particular case of cubic WN with a random distribution of vacancies with a concentration  $C_v$  on both sublattices (keeping the W-to-N ratio constant), a perfectly random structure exhibits a probability  $p(r) = \{6!/r!(6-r)!\}(1-C_v)^r C_v^{(1-r)}$  of finding  $r$  nearest-neighbor nitrogen atoms for each W atom. Our analysis finds that these expected probabilities are within the range of the randomly generated configurations reported in this paper. For example, for the five configurations with  $C_v = 0.25$ , the fraction of W atoms that have  $r = 6, 5, 4,$  and  $3$  nitrogen nearest neighbors range from 0.04–0.25, 0.25–0.46, 0.29–0.42, and 0.08–0.17, respectively. Each of these ranges includes the expected value for a perfectly random structure  $p(r) = 0.18, 0.36, 0.30,$  and  $0.13$ , respectively, while the mean values from the five simulated structures, 0.13, 0.38, 0.34, and 0.13 are also in agreement with the expected probabilities.

### III. RESULTS AND DISCUSSION

USPEX calculations for identifying the thermodynamically stable phase for WN at the 1:1 composition indicate that the NbO phase of WN is the most stable phase, with a formation enthalpy per formula unit  $H_f = -0.839$  eV. Other phases of WN that are thermodynamically close to the NbO phase are the monoclinic and rhombohedral phases of WN, with formation enthalpies of  $-0.701$  and  $-0.21$  eV, respectively. The unit cell of the monoclinic phase contains 2 W and 2 N atoms and exhibits lattice parameters of 7.211, 2.922, and 4.303 Å at angles of  $90^\circ, 102^\circ,$  and  $90^\circ$ , while the corresponding values for the rhombohedral unit cell with also two atoms of each type are 2.953, 2.953, and 9.513 Å at  $120^\circ, 90^\circ,$  and  $90^\circ$ .

Figure 1 directly compares unit cells and charge distributions of WN in the rocksalt and the NbO structures. Schematics of their conventional unit cells are shown in Figs. 1(a) and 1(b), respectively, illustrating the similarity of the two structures. The conventional unit cell of the rocksalt phase belongs to the space group 225 ( $Fm-3m$ ) with W and N atoms occupying the Wyckoff positions  $4a$  (0,0,0) and  $4b$  (0.5,0.5,0.5). The NbO phase belongs to the space group 221 ( $Pm-3m$ ) with W atoms occupying the Wyckoff positions  $3c$  (0.5,0.5,0.0), while N atoms occupy the Wyckoff positions  $3d$  (0.0,0.0,0.5). Therefore, the NbO phase can be directly derived from the rocksalt phase by introducing a regular array of vacancies along  $\langle 111 \rangle$  directions, leading to 25% vacancies on both anion and cation sublattice sites, and a reduction in the number of nearest neighbors from six for the NaCl structure to four for the NbO structure. The introduction of the regular array of vacancies leads to a 5% reduction in the calculated lattice constant from 4.357 Å for the NaCl structure to 4.125 Å for the NbO structure, as also summarized in Table I. Correspondingly, the unit-cell volume for the NbO structure is 15% smaller than for the NaCl structure. However, it also contains 25% less atoms, such that WN in the NbO structure has a 12% smaller density than in the NaCl structure.

Figures 1(c) and 1(d) show electron-density difference contour maps of the (001) basal plane of WN in the NaCl and NbO structures, respectively. The plotted electron density difference  $\rho$ , plotted in units of electrons per Å<sup>3</sup>, is obtained by subtracting the atomic charge distribution from the calculated charge distribution of WN in its respective structure as described in Sec. II. That is, the blue areas

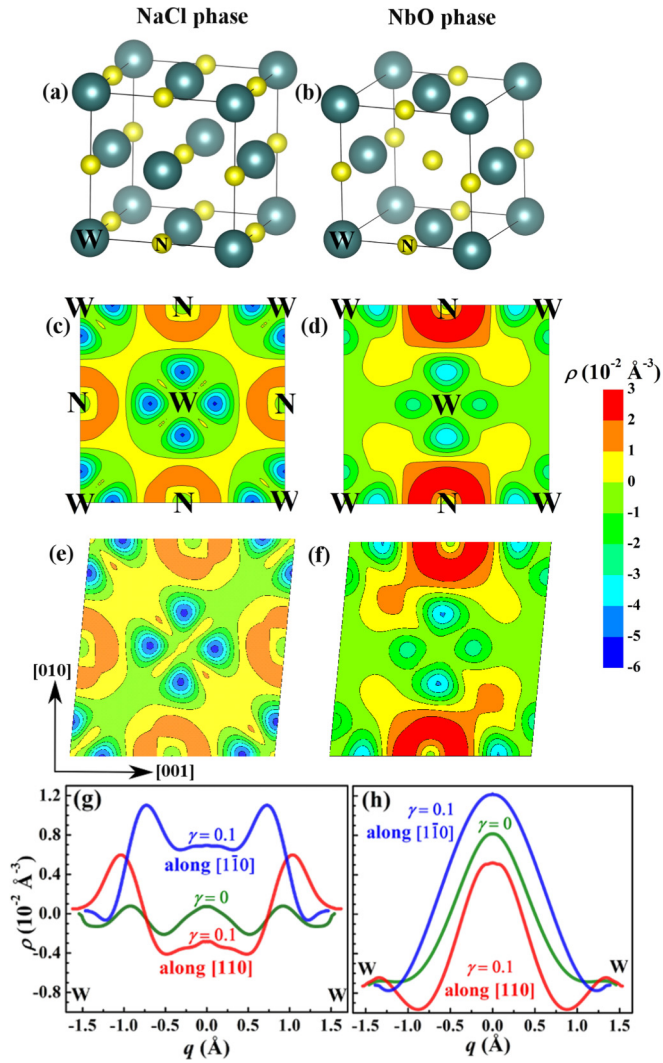


FIG. 1. Schematic of the conventional (a) rocksalt and (b) NbO structure unit cell. Contour plot of electron density difference  $\rho$  in units of electrons per  $\text{\AA}^3$ , in the basal plane of the (c) rocksalt and (d) NbO structure and [(e),(f)] corresponding plots with  $\gamma = 0.1$  shear strain. Line plots of  $\rho$  along  $\langle 110 \rangle$  directions with and without shear strain in the (g) rocksalt and (h) NbO phase.

in the plots correspond to a positive charge indicating the depletion of electrons in comparison to the electron density for noninteracting atoms, while the red areas indicate an increase in the electron density. The most prominent features in the plot in Fig. 1(c) are the dark-blue areas near the W atoms along  $\langle 100 \rangle$  directions, indicating the depletion of electrons with a minimum of  $\rho = -0.051 \text{ \AA}^{-3}$ , corresponding to the reduction of the electron density by 0.051 electrons per  $\text{\AA}^3$ , and the

circular rings of an elevated electron density  $\rho = 0.015 \text{ \AA}^{-3}$  around the N atoms. This corresponds to an electron transfer from the  $d$  orbitals of the W atoms to the  $p$  orbitals of the N atoms, which is a result of the  $p$ - $d$  sigma bonding. The corresponding charge distribution map for WN in the NbO structure in Fig. 1(d) has similar features, however, the electron depletion near the W atoms is less pronounced, with a minimum of  $\rho = -0.04 \text{ \AA}^{-3}$ , while the increase of the electron density around the N atoms of  $\rho = 0.027 \text{ \AA}^{-3}$  is stronger than for the NaCl structure. This suggests a stronger electron transfer into N  $2p$  orbitals and a correspondingly stronger  $p$ - $d$  sigma bonding for the NbO structure than for the NaCl structure, which we attribute to a combination of the smaller number of atoms per unit cell and the smaller W-N bond distance.

Figures 1(e) and 1(f) show charge distribution maps of sheared unit cells in order to explore changes in atomic bonding and the related mechanical stability. More specifically, the plot in Fig. 1(e) shows the electron-density difference of the (001) basal plane of a rocksalt structure WN unit cell for which a 10% shear strain is applied to the (010) plane along the [100] direction. This plot shows, similar to the unstrained map in Fig. 1(c), an electron depletion along the W-N bond near W atoms and an increased electron density around the N atoms. In addition, areas with a relatively low electron density difference [labeled in green in Fig. 1(e)] extend along the  $[110]$  direction between neighboring W atoms, while a high electron density difference with a maximum of  $\rho = 0.011 \text{ \AA}^{-3}$  develops in the perpendicular  $[1\bar{1}0]$  direction. That is, shearing causes electron migration from the  $[110]$  to the  $[1\bar{1}0]$  axes between W atoms, which we attribute to an asymmetric occupation of W  $d$ - $t_{2g}$  orbitals which is the primary reason for the mechanical instability of WN in the rocksalt structure, as discussed in more detail below. The corresponding charge distribution map in Fig. 1(f) from the strained NbO structure also indicates an increase in the electron density along the  $[1\bar{1}0]$  direction between neighboring W atoms, while the remainder of the charge distribution is similar to the unstrained case shown in Fig. 1(d).

Figures 1(g) and 1(h) further illustrate the charge transfer in W  $d$ - $t_{2g}$  orbitals during shear deformation. They are plots of the electron-density difference along  $\langle 110 \rangle$  directions between neighboring W atoms for the NaCl and NbO structures, respectively. The curve labeled  $\gamma = 0$  in Fig. 1(g) is the electron density difference  $\rho$  in unstrained NaCl structure WN plotted vs the distance  $q$  from the center between two W atoms along  $\langle 110 \rangle$  directions. This curve is for both  $[110]$  and  $[1\bar{1}0]$  directions that exhibit the same  $\rho(q)$  which oscillates around  $\rho = 0$  with a minimum of  $-0.002 \text{ \AA}^{-3}$  at  $q = -0.52 \text{ \AA}$  and a maximum of  $7 \times 10^{-4} \text{ \AA}^{-3}$  at the midpoint of the two W

TABLE I. The WN lattice constant  $a$ , bulk modulus  $B$ , cubic elastic tensor elements  $C_{11}$ ,  $C_{12}$ , and  $C_{44}$ , isotropic elastic constant  $E$ , isotropic shear modulus  $G$ , and isotropic Poisson's ratio  $\nu$ , determined from first-principles density functional theory calculations.

Phase	$a(\text{\AA})$	$B(\text{GPa})$	$C_{11}(\text{GPa})$	$C_{12}(\text{GPa})$	$C_{44}(\text{GPa})$	$E(\text{GPa})$	$G(\text{GPa})$	$\nu$
NbO	4.125	349	796	126	175	560	228	0.23
Rocksalt (NaCl)	4.357	361	680	201	-86	-285	-73	0.95

atoms ( $q = 0 \text{ \AA}$ ). In contrast, the red curve in Fig. 1(g), which shows  $\rho$  along [110] for a shear strain  $\gamma = 0.1$ , indicates an electron depletion in the middle between the W atoms, with  $\rho = -0.004 \text{ \AA}^{-3}$  for  $q = \pm 0.48 \text{ \AA}$ , and exhibits peaks of  $\rho = 0.006 \text{ \AA}^{-3}$  at  $q = \pm 1.03 \text{ \AA}$ , corresponding to a high electron density at a distance of  $0.59 \text{ \AA}$  from the W atoms. The corresponding  $\rho(q)$  curve for the  $[1\bar{1}0]$  direction indicates a considerably higher overall electron density, with peaks of  $\rho = 0.011 \text{ \AA}^{-3}$  at  $0.73 \text{ \AA}$  from the W atoms, and a relatively high  $\rho$  of  $0.007 \text{ \AA}^{-3}$  in the center between two W atoms. In summary, shear strain of WN in the rocksalt structure causes a considerable accumulation of electron density in the  $\langle 110 \rangle$  directions between W atoms, indicating filling of W  $d$ - $t_{2g}$  orbitals and, for the  $[1\bar{1}0]$  direction for which the W-W interatomic distance decreases, also a considerable electron density along the entire W-W bond, suggesting orbital overlap and much increased strength of the metal-metal bond. In contrast,  $\rho$  along the [100] direction between W and N atoms (not shown) shows relatively little change upon application of a shear strain, exhibiting a maximum of  $0.015 \text{ \AA}^{-3}$  and a minimum of  $-0.051 \text{ \AA}^{-3}$  at  $1.57$  and  $0.67 \text{ \AA}$  from the W atom in the absence of shear, which vary just slightly to  $0.016 \text{ \AA}^{-3}$  and  $-0.052 \text{ \AA}^{-3}$  with a shear strain of 10%.

Figure 1(h) shows the  $\rho(q)$  curves along  $\langle 110 \rangle$  directions for WN in the NbO structure. The  $\gamma = 0$  curve indicates considerable electron accumulation at the center between W atoms, with a maximum of  $\rho = 0.008 \text{ \AA}^{-3}$ , while the electron density is depleted near the W atoms with  $\rho = -0.007 \text{ \AA}^{-3}$ . This suggests considerable bonding between tungsten atoms in the unstrained NbO structure, in strong contrast to the unstrained NaCl structure, which has almost no charge transfer along W-W bond directions, as discussed above. We attribute the W-W bonding in the NbO structure to the reduced number of W nearest neighbors from 12 for the NaCl structure to eight in the NbO structure, and also to the 5% smaller interatomic distance which facilitates orbital overlap. An applied shear strain to WN in the NbO structure results in a reduction of the electron density along nearly the entire [110] direction between W atoms, as indicated by the red curve in Fig. 1(h), while the  $\rho(q)$  curve along  $[1\bar{1}0]$  (blue curve) shows an increase in the electron density. The magnitude of this increase is comparable to the magnitude of the decrease along [110], suggesting that an increase in bond strength along  $[1\bar{1}0]$  is approximately compensated by a decrease in bond strength along [110], resulting in a negligible net effect for shear of the WN in the NbO structure due to the  $t_{2g}$  states. This is in strong contrast to the NaCl structure, where shear results in a net increase in the strength of W-W bonds, which causes mechanical instability, as discussed below.

Table I lists the calculated elastic constants for WN in the NaCl and NbO structures. The bulk modulus  $B = 349$  GPa for the NbO structure is slightly (3%) smaller than  $B = 361$  GPa for the NaCl structure, which may be attributed to the higher density of the NaCl structure. In contrast,  $C_{11}$  for the NbO structure is 17% larger than for the rocksalt phase, which we attribute to the more pronounced electron transfer to the N atoms as shown in Fig. 1(d) and discussed above, leading

to stronger and 5%-shorter anion-cation bonds along  $\langle 100 \rangle$  directions and a correspondingly higher  $C_{11}$ . Consistent with these arguments,  $C_{12} = 126$  GPa for the NbO structure is 37% smaller than  $C_{12} = 201$  GPa for the NaCl structure. The stark contrast between the two phases emerges when comparing  $C_{44}$ , which is 175 GPa for the NbO structure but  $-86$  GPa (negative) for the NaCl structure. That is, WN in the NaCl structure is mechanically unstable against shear deformation, as mechanical stability requires  $C_{11} > 0$ ,  $C_{11} + 2C_{12} > 0$ , and  $C_{44} > 0$  [59]. We attribute the negative  $C_{44}$  value to a considerable charge transfer into W  $d$ - $t_{2g}$  orbitals, as presented in Figs. 1(e) and 1(g), which results in orbital overlap along W-W bond directions, leading to an increasing W-W bond strength and therefore a reduction in the energy for WN in the NaCl structure upon application of a shear strain. In addition to the mechanical instability, the NaCl structure is also thermodynamically unstable against phase separation into metallic W and molecular  $N_2$ , with a calculated enthalpy of formation of  $0.623$  eV per formula unit. In contrast, WN in the NbO structure has a negative formation enthalpy of  $-0.839$  eV per formula unit and is therefore thermodynamically stable. Table I also lists the isotropic elastic modulus  $E$  and the isotropic shear modulus  $G$ , determined from  $C_{11}$ ,  $C_{12}$ , and  $C_{44}$  using Hill's method [53]. The calculated Pugh's ratio  $k = G/B = 0.65$  and the Poisson's ratio  $\nu = 0.23$  suggests that WN in the NbO structure is brittle, as a common criterion for ductility of a material is  $k < 0.6$  and  $\nu > 0.25$  [54].

To further investigate the reasons for the mechanical instability and stability of WN in the rocksalt and NbO phases, we analyze and compare the electronic DOS. Figure 2(a) is a plot of the total DOS vs the energy  $E = -11$  to  $1.5$  eV for a conventional unit cell of WN in the NaCl structure. The red curve for the unstrained ( $\gamma = 0$ ) structure increases from 0 at  $E = -10.89$  eV to a maximum of  $20.2$  states per eV at  $E = -7.36$  eV and drops to  $0.5 \text{ eV}^{-1}$  at  $E = -4.79$  eV, followed by an approximately linear increase to  $4.7 \text{ eV}^{-1}$  at the Fermi level ( $E = 0$  eV). An analysis based on the site projected DOS reveals that the feature from  $E = -11$  eV to  $-5$  eV can be primarily attributed to the N  $2p$  orbitals and the W  $e_g$  ( $d_{x^2-y^2}$  and  $d_{z^2}$ ) states with only a small W  $t_{2g}$  contribution, while the region from  $-5$  eV to the Fermi level consists primarily of the W  $t_{2g}$  ( $d_{xy}$ ,  $d_{yz}$ , and  $d_{xz}$ ) states and the peak at  $0.26$  eV above  $E_f$  is due to the empty W  $6s$  states. Further analysis indicates that 70% of occupied W  $d$  states have  $t_{2g}$  character, while the remaining 30% are  $e_g$ .

The blue curve in Fig. 2(a) is the corresponding DOS plot for the NaCl structure with an applied  $\gamma = 0.1$  shear strain. The curve shows overall the same features as the relaxed DOS, with a peak of  $15 \text{ eV}^{-1}$  at  $E = -7.36$  eV and a linear increase for  $E > -4$  eV. However, the Fermi level is  $0.14$  eV below  $E_f$  of the relaxed structure, as indicated by the blue dotted vertical line at  $E = -0.14$  eV. Also, the DOS valley that is observed for the relaxed structure between  $E = -8.7$  and  $-8.1$  eV is removed for the strained case, causing an increase of  $0.6$  states in this energy range. Furthermore, the application of shear results in a decrease of  $1.4$  states in the energy range  $E = -8.1$  to  $-7$  eV and an increase of  $0.9$  states in the energy range  $E = -7$  to  $-5$  eV, while the DOS for  $E = -11$  to  $-8.7$  eV remains nearly unaffected by the shear strain. An analysis based on site projected DOS indicates that the

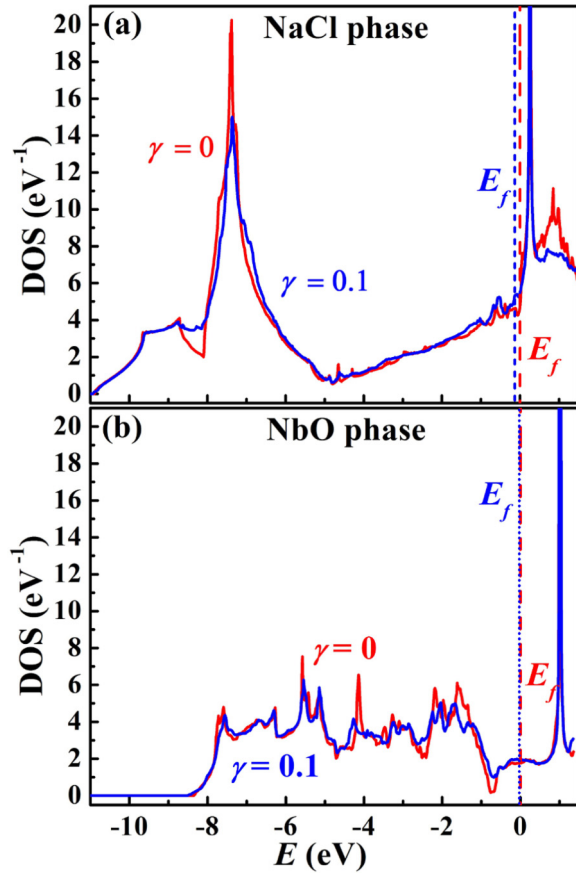


FIG. 2. Total electron density of states of conventional unit cells of (a) the rocksalt phase and (b) the NbO phase of WN, in their cubic ( $\gamma = 0$ ) state or with a 10% shear strain ( $\gamma = 0.1$ ).

additional states for  $E = -8.7$  to  $-8.1$  eV exhibit  $t_{2g}$  character, while those between  $-7$  and  $-5$  eV have  $e_g$  character. This implies that, during shearing,  $t_{2g}$  states move from the energy range  $E = -8.1$  to  $-7$  eV to deeper energies, filling the valley at  $E = -8.7$  to  $-8.1$  eV, which results in a lowering of the total energy and therefore contributes to the increase in stability during shearing. In contrast,  $e_g$  states move to the right, populating states of higher binding energies of  $E = -7$  to  $-5$  eV, which compensates some of the effect from the  $t_{2g}$  states. Also, the reduction of the Fermi level by 0.14 eV upon 10% shear strain corresponds to a cumulative 0.6 states per conventional unit cell with primarily  $t_{2g}$  character to migrate from states near the Fermi level ( $E = -0.14$  to  $0$  eV) to new states with lower binding energies in the region  $E = -5$  to  $-0.14$  eV. In summary, we attribute the mechanical instability of WN in the rocksalt structure to the energy reduction of W  $t_{2g}$  states upon shearing, as manifested by a Fermi-level shift as well as an increase in the DOS that effectively removes a DOS valley between  $E = -8.7$  and  $-8.1$  eV. This energy reduction corresponds to a real-space migration of electrons from the longer [110] to the shorter [1 $\bar{1}$ 0] W-W bonds, as discussed above. In contrast, electrons in  $e_g$  states partially compensate the energy reduction as they move to higher energies, causing a resistance against shear which is attributed to  $W e_g - N p$  sigma bonds which are disrupted by the shear deformation.

Figure 2(b) shows the DOS of WN in the NbO phase with the Fermi level of the unstrained unit cell set to zero. The DOS for the relaxed structure ( $\gamma = 0$ ) plotted as a red curve exhibits a broad feature from  $-8$  to  $-1$  eV with a noisy but overall relatively constant average DOS of  $3.6 \text{ eV}^{-1}$ , followed by a drop to a minimum at  $-0.76$  eV and a  $\text{DOS}(E_f) = 1.8 \text{ eV}^{-1}$ , while the sharp peak of the empty W  $6s$  states is at  $E = 1.00$  eV. A site projected DOS analysis indicates that the entire occupied DOS region from  $E = -8.34$  eV to the Fermi level exhibits a mixed W  $t_{2g}$ , W  $e_g$ , and N  $p$  orbital character. There are no detectable trends with  $E$ , with the partial DOS remaining approximately constant at  $0.70 \text{ eV}^{-1}$  for W  $t_{2g}$ ,  $0.45 \text{ eV}^{-1}$  for W  $e_g$ , and  $1.04 \text{ eV}^{-1}$  for N  $p$  between  $-8$  and  $-1$  eV. Therefore, the fraction of W  $d$  electrons occupying  $e_g$  vs  $t_{2g}$  orbitals is 40%:60%. That is, the NbO structure has a higher occupation of  $e_g$  orbitals (40%) than the NaCl structure (30%), which may explain the higher  $C_{11}$  and larger charge transfer along [100] discussed above.

The blue curve in Fig. 2(b) is the corresponding DOS of WN in the NbO phase with 10% shear strain ( $\gamma = 0.1$ ). This curve exhibits features similar to the unstrained case with the same average DOS of  $3.6 \text{ eV}^{-1}$  between  $-8$  and  $-1$  eV, and a minimum at  $-0.69$  eV. The Fermi level is also nearly unaffected by the strain, as indicated by the blue dotted line at  $-0.03$  eV. Shearing causes only minor differences in the DOS. In particular, the DOS peaks at  $-4.1$  and  $-1.6$  eV as well as the DOS valleys at  $-2.5$  and  $-0.8$  eV are partially or completely removed upon shearing, causing 0.3 and 0.1 electrons per conventional cell moving from  $-4.1$  to  $-2.5$  eV and from  $-1.6$  to  $-0.8$  eV, respectively, which results in a net energy increase. The corresponding bond weakening is attributed to the depletion of electrons from W-W [110] bond axes and the disruption of the  $e_g - N p$  sigma bonds. However, this electron migration is considerably smaller than in the case of the NaCl structure, consistent with the plots in Figs. 1(g) and 1(h).

Figure 3 summarizes the results from supercell calculations which explore the property changes of stoichiometric cubic WN as a function of vacancy concentration  $C_v = 0\% - 28.125\%$ , where  $C_v = 0$  and  $0.25$  correspond to the NaCl and NbO structures, respectively. The composition is kept constant, that is, the N-to-W ratio is unity for all simulated configurations. The plot in Fig. 3(a) shows the calculated enthalpy of formation  $H_f$  per formula unit for multiple atomic arrangements for each  $C_v$  value. The different symbols indicate the different methods from which the configurations were created, including vacancies on the NbO structure sublattice and ordered and random structures, as described in detail in Sec. II. The data point at  $C_v = 0$  with a formation enthalpy  $H_f = 0.623$  eV is for WN in the NaCl structure. As discussed above, the positive value indicates thermodynamic instability against phase separation into metallic tungsten and molecular nitrogen. Increasing  $C_v$  to 3.125%, which corresponds to a single vacancy pair within the 64 site supercell, results in a steep drop in  $H_f$  to 0.018 eV. This considerable energy drop is an indication of the instability of the rocksalt structure against the formation of anion and cation vacancy pairs, that is, Schottky defects. The most stable configuration for  $C_v = 3.125\%$ , indicated by an open circle in Fig. 3(a), corresponds to a configuration with the W and N vacancies

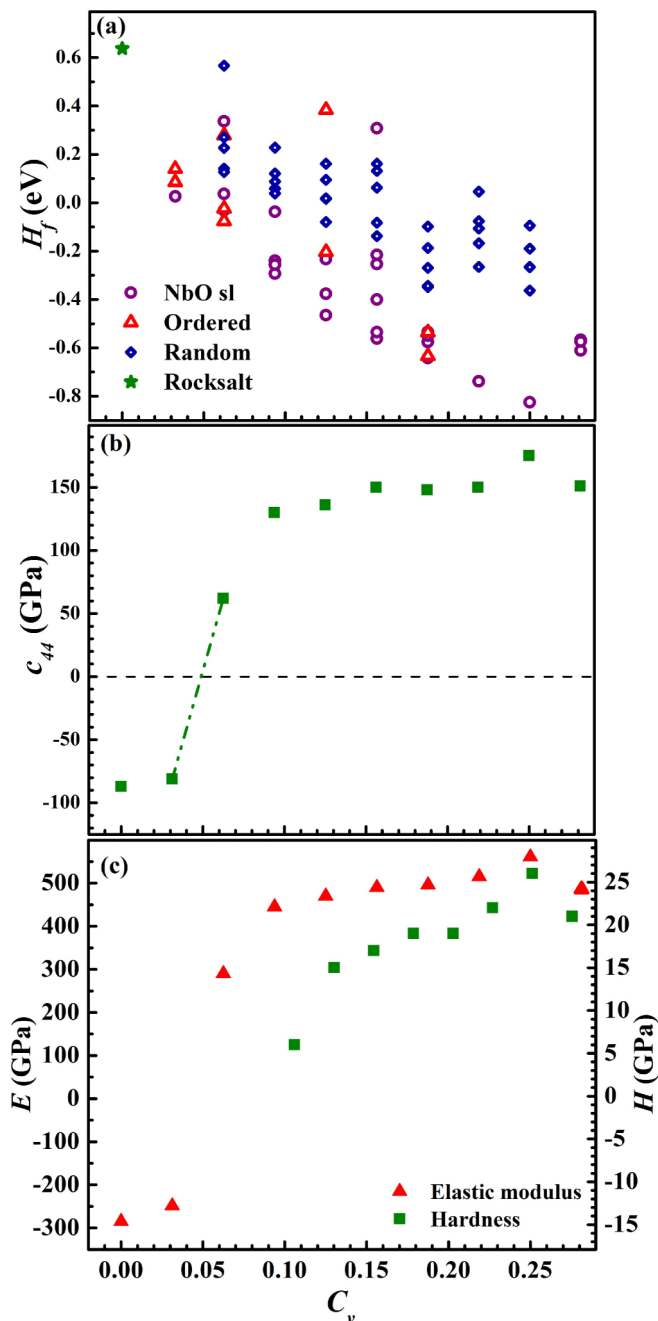


FIG. 3. (a) The WN formation enthalpy  $H_f$  vs vacancy concentration  $C_v$  with vacancies arranged on the NbO sublattice (sl) or on ordered or random sites. (b)  $C_{44}$  and (c) isotropic elastic modulus  $E$  and hardness  $H$ , of the lowest-energy configuration of WN for each  $C_v$ .

separated along the [111] direction by 3.76 Å, occupying the NbO sublattice positions (0,0,0) and (0.5,0.5,0.5) measured in units of the lattice constant. Other configurations with the same  $C_v = 3.125\%$ , and with the W vacancy at the origin and the N vacancy occupying (0.5,0,0), (1,0.5,0), or (1,0.5,1) yielding intervacancy distances of 2.17, 4.88, and 6.50 Å, respectively, have calculated enthalpies that are 0.099, 0.045, and 0.045 eV higher, as indicated by open triangles in the figure. The largest value for the configuration with

the smallest vacancy separation indicate that vacancy pairs on nearest-neighbor cation and anion sites are energetically unfavorable, suggesting short-range vacancy repulsion. For  $C_v = 6.25\%$ , the plot shows  $H_f$  values of nine vacancy arrangements including (i) five configurations indicated by open diamonds for which vacancies are placed randomly on two cation and two anion sites of the 64-atom supercell, (ii) two configurations indicated by open circles for which the vacancies are located on sites of the vacancy sublattice of the NbO structure, and (iii) three manually chosen ordered configurations indicated by triangles. The lowest-energy configuration exhibits relatively large spacings between all anion and cation vacancies with the two W vacancies occupying the positions (0,0,0) and (1,1,0), and the N vacancies at (0,0.5,1) and (1,1.5,1). The  $H_f = -0.09$  eV is negative, indicating thermodynamic stability against phase separation into tungsten and molecular nitrogen. We note, however, this configuration is not thermodynamically stable against transformation into the NbO structure. Increasing  $C_v$  further leads to a continuous decrease in  $H_f$  of the lowest-energy configurations, reaching  $-0.447$  eV for  $C_v = 12.5\%$  and  $-0.839$  eV for  $C_v = 25\%$ , where the latter corresponds to the formation enthalpy of WN in the NbO phase. For  $C_v \geq 9.375\%$ , all lowest-energy configurations are derived from the NbO structure, that is, the cation and anion vacancies occupy sites which are also vacant in the NbO structure. This suggests, consistent with the previous observations, that vacancies preferentially arrange in such a way that each W (N) atom has at least four N (W) neighbors, as is the case in the NbO structure, while anion-cation vacancy pairs on neighboring sites are energetically unfavorable. Correspondingly, the randomly chosen configurations all have considerably higher enthalpies, which is attributed to them containing some vacancies on nearest-neighbor sites. Consistent with this argument, all simulated configurations with  $C_v > 25\%$  have higher  $H_f$  values than the NbO structure, since they all contain at least one nearest-neighbor vacancy pair. This is illustrated in Fig. 3(a) with the data points for  $C_v = 28.125\%$ , which are from four simulated configurations that contain all vacancies of the NbO structure plus an additional W and N vacancy pair. Their enthalpies are  $H_f = -0.611$ ,  $-0.572$ ,  $-0.573$ , and  $-0.567$  eV. That is, the lowest enthalpy for  $C_v = 28.125\%$  is 0.228 eV per formula unit higher than for the NbO structure. This further corroborates USPEX calculation results indicating that the thermodynamically most stable phase for stoichiometric WN is the NbO structure. We reiterate here that none of the phases are thermodynamically stable against transformation into WN in the NbO structure. However, kinetic barriers for vacancy diffusion within cubic WN likely inhibit the formation of the perfect vacancy lattice of the NbO phase, such that cubic WN with a  $C_v < 25\%$  is likely to form. We also note that all calculated configurations exhibit a finite DOS at the Fermi level, predicting metallic conduction for stoichiometric cubic WN, independent of  $C_v$ .

Figure 3(b) is a plot of  $C_{44}$ , the shear modulus for {001} planes applied along (100) directions, as a function of  $C_v$  for the configurations which have the lowest  $H_f$  for each given vacancy concentration. As already discussed above, WN in the NaCl structure has a negative  $C_{44} = -86$  GPa. Increasing  $C_v$  causes initially a slight increase to  $-81$  GPa for  $C_v = 3.125\%$ ,

followed by a steep increase to 62 GPa for  $C_v = 6.25\%$  and 130 GPa for  $C_v = 9.375\%$ , then a gradual continued increase to reach a maximum of 175 GPa for the NbO structure with  $C_v = 25\%$  and a decrease to 151 GPa for  $C_v = 28.125\%$ . A linear interpolation between  $C_v = 3.125$  and  $6.25\%$ , as shown with the dotted line in Fig. 3(b), indicates that  $C_{44}$  transitions from negative to positive at  $C_v = (5 \pm 1)\%$ . That is, cubic WN is mechanically unstable for  $C_v < 5\%$  and stable for  $C_v > 5\%$ . The Pugh's ratio, determined from the isotropic  $G$  and  $B$  as described in Sec. II, increases from  $-0.117$  to  $0.65$ , indicating decreasing ductility with increasing vacancy concentration as we move from the NaCl to the NbO phase, which is consistent with the increasing  $C_{44}$ .

Figure 3(c) is a plot of the calculated isotropic elastic modulus  $E$  and hardness  $H$  as a function of vacancy concentration. They are calculated for the cubic WN configurations with the lowest  $H_f$  for each given  $C_v$  value presented in Fig. 3(a). The  $E$  and  $H$  values are determined from the calculated stiffness constants  $C_{ij}$ , as described in detail in Sec. II. The rocksalt phase ( $C_v = 0$ ) has a negative elastic modulus  $E = -285$  GPa, consistent with its mechanical instability. An initial increase in vacancy concentration to  $C_v = 3.125\%$  causes a small increase to  $E = -249$  GPa, consistent with the  $C_{44}$  vs  $C_v$  shown above. A further increase in  $C_v$  results in a steep increase to 290 GPa at  $C_v = 6.25\%$  and 445 GPa at  $C_v = 9.375\%$ . Beyond this concentration,  $E$  gradually increases to  $E = 470$  GPa at  $C_v = 12.5\%$  and to  $E = 561$  GPa for the NbO phase at  $C_v = 25\%$ , and finally decreases to  $E = 486$  GPa for  $C_v = 28.125\%$ . Consistent with the critical vacancy concentration for  $C_{44}$  discussed above, we conclude that  $E = 0$  at  $C_v = (5 \pm 1)\%$ .

The corresponding hardness values obtained using Tian's model [55] are also shown in Fig. 3(b). They increase steeply from zero at  $C_v = 5 \pm 1\%$  to  $H = 6$  GPa for  $C_v = 6.25\%$  to  $H = 15$  GPa at  $C_v = 9.375\%$ , and then more slowly to 17 GPa at 12.5% and  $H = 26$  GPa for the NbO phase at  $C_v = 25\%$  and decreases to 21 GPa for  $C_v = 28.125\%$ . The values are not plotted for  $C_v \leq 3.125\%$ , because  $G$  is negative. We note that using Chen's model [60] to determine the hardness results in slightly ( $1 \pm 1$  GPa) lower values for all  $C_v$  than the plotted data obtained with Tian's model [55]. The weakest ideal tensile strength of the NbO phase of WN, at  $C_v = 0.25$ , is calculated to be 49 GPa along the  $\langle 001 \rangle$  direction, while the ideal strengths along  $\langle 110 \rangle$  and  $\langle 111 \rangle$  are 71 and 96 GPa, respectively. Correspondingly, the weakest ideal shear strength is calculated to be 29 GPa along  $(111) [11\bar{2}]$ , while it is 41 GPa along  $(010) [001]$ . This lowest ideal shear strength of 29 GPa is in reasonable agreement with the predicted hardness of 26 GPa using Tian's model, supporting the approach of using Tian's model to estimate the hardness of WN.

The predicted elastic moduli vs  $C_v$  curve in Fig. 3(c) can be compared with previously reported experimental values for nearly stoichiometric WN compositions which range from 240 to 430 GPa [21,36–38]. Linear interpolation of our predicted moduli indicates that  $E = 240$  and 430 GPa

correspond to  $C_v = 6\%$  and  $9\%$ . That is, the large range of reported elastic moduli can be explained by a relatively modest variation in vacancy concentration, from 6% to 9%. Our calculations predict, using a linear interpolation of  $H$  vs  $C_v$ , a hardness that increases from 5 to 14 GPa for this range  $C_v = 6\% - 9\%$ , which is in reasonable agreement with the corresponding reported range  $H = 5 - 30$  GPa from experimental measurements [25,31,36–40], where the large  $H > 26$  GPa may be due to microstructural effects including hardening due to grain boundaries or residual compressive stress. We note that the large  $E = 561$  GPa predicted for WN in the NbO phase is considerably larger than reported elastic moduli. This is, in fact, consistent with the absence of any experimental report on WN in the NbO phase. We attribute the difficulty in the experimental growth of the NbO phase to kinetic barriers for cation and/or anion vacancy diffusion, which is required to form the regular array of vacancies that the NbO phase exhibits.

#### IV. CONCLUSIONS

Rocksalt phase WN is both thermodynamically and mechanically unstable. The mechanical instability is due to a negative shear modulus, with a calculated  $C_{44} = -86$  GPa. The instability against shear is attributed to significant electron rearrangement in W  $d-t_{2g}$  orbitals. More specifically, shear causes orbital overlap between neighboring W atoms, leading to an energy reduction in the bonding orbitals and, in turn, a lower total energy. In contrast, WN in the NbO phase exhibits a smaller electron rearrangement of the  $t_{2g}$  orbitals and a positive  $C_{44} = 175$  GPa. The transition from the unstable NaCl structure to the stable NbO structure is explored using supercell calculations for which the N-to-W ratio is kept at 1.0, but the vacancy concentration is increased from  $C_v = 0\%$  for the NaCl structure to  $C_v = 25\%$  for the NbO structure. The formation enthalpy per formula unit decreases from  $H_f = 0.623$  to  $-0.839$  eV as  $C_v$  increases from 0% to 25%, while the isotropic elastic modulus increases from  $E = -285$  to 561 GPa and the material becomes less ductile. At a critical vacancy concentration  $C_v = 5\%$ ,  $C_{44}$  is zero which also causes  $E = H = 0$ . Thus, the rocksalt phase of WN is unstable for  $C_v < 5\%$ , but becomes mechanically stable for  $C_v > 5\%$ . Both  $E$  and  $H$  increase steeply with  $C_v = 5\% - 10\%$ . Therefore, the large range of previously reported values for  $E$  can be attributed to a modest change in  $C_v$  from 6% to 9%.

#### ACKNOWLEDGMENTS

The authors acknowledge support by the National Science Foundation under Grants No. 1309490, No. 1537984, No. 1234872, No. 1234777, No. 1629230, and No. 1629239. Computational resources were provided by the Center for Computational Innovations at RPI.

[1] L. Hultman, *Vacuum* **57**, 1 (2000).

[2] J. Musil, *Surf. Coatings Technol.* **125**, 322 (2000).

[3] K. Zhang, K. Balasubramanian, B. D. Ozsdolay, C. P. Mulligan, S. V. Khare, W. T. Zheng, and D. Gall, *Surf. Coatings Technol.* **277**, 136 (2015).

- [4] Z. T. Y. Liu, D. Gall, and S. V. Khare, *Phys. Rev. B* **90**, 134102 (2014).
- [5] Z. T. Y. Liu, X. Zhou, S. V. Khare, and D. Gall, *J. Phys.: Condens. Matter* **26**, 025404 (2014).
- [6] H. S. Seo, T. Y. Lee, J. G. Wen, I. Petrov, J. E. Greene, and D. Gall, *J. Appl. Phys.* **96**, 878 (2004).
- [7] C.-S. Shin, D. Gall, P. Desjardins, A. Vailionis, H. Kim, I. Petrov, J. E. Greene, and M. Odén, *Appl. Phys. Lett.* **75**, 3808 (1999).
- [8] S. Koseki, K. Inoue, S. Morito, T. Ohba, and H. Usuki, *Surf. Coatings Technol.* **283**, 353 (2015).
- [9] M. Yasuoka, P. Wang, and R. Murakami, *Surf. Coatings Technol.* **206**, 2168 (2012).
- [10] E. E. Vera, M. Vite, R. Lewis, E. A. Gallardo, and J. R. Laguna-Camacho, *Wear* **271**, 2116 (2011).
- [11] R. R. Manory, S. Mollica, L. Ward, K. P. Purushotham, P. Evans, J. Noorman, and A. J. Perry, *Surf. Coatings Technol.* **155**, 136 (2002).
- [12] Y.-L. Su and T.-H. Liu, *Vacuum* **77**, 343 (2005).
- [13] X. Chen, J. Xu, and Q. Xiao, *Int. J. Refract. Met. Hard Mater.* **52**, 143 (2015).
- [14] D. G. Sangiovanni, V. Chirita, and L. Hultman, *Thin Solid Films* **520**, 4080 (2012).
- [15] D. G. Sangiovanni, L. Hultman, and V. Chirita, *Acta Mater.* **59**, 2121 (2011).
- [16] H. Kindlund, D. G. Sangiovanni, J. Lu, J. Jensen, V. Chirita, J. Birch, I. Petrov, J. E. Greene, and L. Hultman, *Acta Mater.* **77**, 394 (2014).
- [17] H. Kindlund, D. G. Sangiovanni, J. Lu, J. Jensen, V. Chirita, I. Petrov, J. E. Greene, and L. Hultman, *J. Vac. Sci. Technol. A* **32**, 030603 (2014).
- [18] D. G. Sangiovanni, V. Chirita, and L. Hultman, *Phys. Rev. B* **81**, 104107 (2010).
- [19] H. Kindlund, D. G. Sangiovanni, L. Martinez-de-Olcoz, J. Lu, J. Jensen, J. Birch, I. Petrov, J. E. Greene, V. Chirita, and L. Hultman, *APL Mater.* **1**, 042104 (2013).
- [20] M. J. Mehl, D. Finkenstadt, C. Dane, G. L. W. Hart, and S. Curtarolo, *Phys. Rev. B* **91**, 184110 (2015).
- [21] B. D. Ozsdolay, C. P. Mulligan, M. Guerette, L. Huang, and D. Gall, *Thin Solid Films* **590**, 276 (2015).
- [22] J. W. Klaus, S. J. Ferro, and S. M. George, *J. Electrochem. Soc.* **147**, 1175 (2000).
- [23] N. Schönberg, *Acta Chem. Scand.* **8**, 204 (1954).
- [24] T. Polcar, N. M. G. Parreira, and A. Cavaleiro, *Wear* **265**, 319 (2008).
- [25] M. Bereznai, Z. Tóth, A. P. Caricato, M. Fernández, A. Luches, G. Majni, P. Mengucci, P. M. Nagy, A. Juhász, and L. Nánai, *Thin Solid Films* **473**, 16 (2005).
- [26] M. L. Addonizio, A. Castaldo, A. Antonaia, E. Gambale, and L. Lemmo, *J. Vac. Sci. Technol. A* **30**, 031506 (2012).
- [27] S. Wang, X. Yu, Z. Lin, R. Zhang, D. He, J. Qin, J. Zhu, J. Han, L. Wang, H. Mao, J. Zhang, and Y. Zhao, *Chem. Mater.* **24**, 3023 (2012).
- [28] J. Qin, X. Zhang, Y. Xue, X. Li, M. Ma, and R. Liu, *Comput. Mater. Sci.* **79**, 456 (2013).
- [29] M. Kavitha, G. Sudha Priyanga, R. Rajeswarapalanichamy, and K. Iyakutti, *J. Phys. Chem. Solids* **77**, 38 (2015).
- [30] Z. T. Y. Liu, X. Zhou, D. Gall, and S. V. Khare, *Comput. Mater. Sci.* **84**, 365 (2014).
- [31] B. D. Ozsdolay, C. P. Mulligan, K. Balasubramanian, L. Huang, S. V. Khare, and D. Gall, *Surf. Coat. Technol.* **304**, 98 (2016).
- [32] S.-H. Jhi, S. Louie, M. Cohen, and J. Morris, *Phys. Rev. Lett.* **87**, 075503 (2001).
- [33] S.-H. Jhi and J. Ihm, *Phys. Rev. B* **56**, 13826 (1997).
- [34] S.-H. Jhi, J. Ihm, S. G. Louie, and M. L. Cohen, *Nature (London)* **399**, 132 (1999).
- [35] S.-H. Jhi, S. G. Louie, M. L. Cohen, and J. Ihm, *Phys. Rev. Lett.* **86**, 3348 (2001).
- [36] T. Polcar and A. Cavaleiro, *Int. J. Refract. Met. Hard Mater.* **28**, 15 (2010).
- [37] E. C. Samano, A. Clemente, J. A. Diaz, and G. Soto, *Vacuum* **85**, 69 (2010).
- [38] P. Hones, N. Martin, M. Regula, and F. Lévy, *J. Phys. D: Appl. Phys.* **36**, 1023 (2003).
- [39] M. Wen, Q. N. Meng, W. X. Yu, W. T. Zheng, S. X. Mao, and M. J. Hua, *Surf. Coatings Technol.* **205**, 1953 (2010).
- [40] T. Yamamoto, M. Kawate, H. Hasegawa, and T. Suzuki, *Surf. Coatings Technol.* **193**, 372 (2005).
- [41] K. Zhang, K. Balasubramanian, B. D. Ozsdolay, C. P. Mulligan, S. V. Khare, W. T. Zheng, and D. Gall, *Surf. Coatings Technol.* **288**, 105 (2015).
- [42] C. Hu, X. Zhang, Z. Gu, H. Huang, S. Zhang, X. Fan, W. Zhang, Q. Wei, and W. Zheng, *Scr. Mater.* **108**, 141 (2015).
- [43] C. S. Shin, D. Gall, N. Hellgren, J. Patscheider, I. Petrov, and J. E. Greene, *J. Appl. Phys.* **93**, 6025 (2003).
- [44] H. Euchner and P. H. Mayrhofer, *Surf. Coatings Technol.* **275**, 214 (2015).
- [45] F. F. Klimashin, H. Euchner, and P. H. Mayrhofer, *Acta Mater.* **107**, 273 (2016).
- [46] H. Euchner, P. H. Mayrhofer, H. Riedl, F. F. Klimashin, A. Limbeck, P. Polcik, and S. Kolozsvari, *Acta Mater.* **101**, 55 (2015).
- [47] J. P. Perdew, K. Burke, and M. Ernzerhof, *Phys. Rev. Lett.* **77**, 3865 (1996).
- [48] J. P. Perdew, J. A. Chevary, S. H. Vosko, K. A. Jackson, M. R. Pederson, D. J. Singh, and C. Fiolhais, *Phys. Rev. B* **48**, 4978 (1993).
- [49] C. W. Glass, A. R. Oganov, and N. Hansen, *Comput. Phys. Commun.* **175**, 713 (2006).
- [50] A. O. Lyakhov, A. R. Oganov, H. T. Stokes, and Q. Zhu, *Comput. Phys. Commun.* **184**, 1172 (2013).
- [51] A. R. Oganov, A. O. Lyakhov, and M. Valle, *Acc. Chem. Res.* **44**, 227 (2011).
- [52] J. Pokluda, M. Černý, M. Šob, and Y. Umeno, *Prog. Mater. Sci.* **73**, 127 (2015).
- [53] R. Hill, *Proc. Phys. Soc., London, Sect. A* **65**, 349 (1952).
- [54] S. F. Pugh, *Philos. Mag. Ser.* **45**, 823 (1954).
- [55] Y. Tian, B. Xu, and Z. Zhao, *Int. J. Refract. Met. Hard Mater.* **33**, 93 (2012).
- [56] K. Momma and F. Izumi, *J. Appl. Crystallogr.* **44**, 1272 (2011).
- [57] P. E. Blöchl, O. Jepsen, and O. K. Andersen, *Phys. Rev. B* **49**, 16223 (1994).
- [58] A. Zunger, S. H. Wei, L. G. Ferreira, and J. E. Bernard, *Phys. Rev. Lett.* **65**, 353 (1990).
- [59] J. Wang, J. Li, S. Yip, D. Wolf, and S. Phillpot, *Physica A* **240**, 396 (1997).
- [60] X. Q. Chen, H. Niu, D. Li, and Y. Li, *Intermetallics* **19**, 1275 (2011).